nature nanotechnology

Article

https://doi.org/10.1038/s41565-023-01401-7

Cell spheroid creation by transcytotic intercellular gelation

Received: 29 December 2021

Accepted: 14 April 2023

Published online: 22 May 2023

Check for updates

Jiaqi Guo[1], Fengbin Wang[2,3,4] ✉, Yimeng Huang[1], Hongjian He[1], Weiyi Tan[1], Meihui Yi[1], Edward H. Egelman[2] ✉ & Bing Xu[1] ✉

Cell spheroids bridge the discontinuity between in vitro systems and in vivo animal models. However, inducing cell spheroids by nanomaterials remains an inefficient and poorly understood process. Here we use cryogenic electron microscopy to determine the atomic structure of helical nanofibres self-assembled from enzyme-responsive D-peptides and fluorescent imaging to show that the transcytosis of D-peptides induces intercellular nanofibres/gels that potentially interact with fibronectin to enable cell spheroid formation. Specifically, D-phosphopeptides, being protease resistant, undergo endocytosis and endosomal dephosphorylation to generate helical nanofibres. On secretion to the cell surface, these nanofibres form intercellular gels that act as artificial matrices and facilitate the fibrillogenesis of fibronectins to induce cell spheroids. No spheroid formation occurs without endo- or exocytosis, phosphate triggers or shape switching of the peptide assemblies. This study—coupling transcytosis and morphological transformation of peptide assemblies—demonstrates a potential approach for regenerative medicine and tissue engineering.

Cell spheroids (for example, organoids[1]), bridging the discontinuity between in vitro systems and in vivo animal models[2–4], are better in vivo microenvironment[5–8] models than two-dimensional layers of cells[9] for mimicking human organs[10,11]. Current procedures for generating spheroids[12–15], such as non-stick substrates, are tedious, time-consuming, costly or poorly controlled. None of these approaches mimics the characteristics of extracellular matrix (ECM) biogenesis, such as regulated precursor secretion and subsequent assembly into matrices[16], to form intercellular junctions[17]. Moreover, ECM proteins contain a variety of post-translational modifications for enzymatic reactions to dynamically regulate cell adhesion[18] and migration[19], such as high frequency of phosphorylation among the identified sites of ECM proteins[20]. Until now, it has been challenging for synthetic materials to mimic the dynamic and transient phosphorylation of ECM proteins. The inherently dynamic architecture of peptide assemblies[21–23] formed by non-covalent interactions may provide a solution, as evidenced by the fact that peptide assemblies form hydrogel matrices to mimic the ECM for cell culture[24,25] and tissue engineering[26–28]. Most of the hydrogels, however, are made ex situ to enclose the cells, which differ from tissues where cells surround the ECM made in situ. We have previously shown that enzyme-responsive D-phosphopeptide assemblies induce HS-5 cell spheroids[29,30], but the detailed mechanism remains obscure. Moreover, despite the diverse functions[31] of peptide nanofibres, their atomic structures remain largely unknown.

Here we report that transcytosis (that is, endocytosis and exocytosis) of enzyme-responsive D-phosphopeptides creates intercellular D-peptide nanofibres as hydrogel matrices to enable cell spheroid formation (Fig. 1a). The protease-resistant D-phosphopeptides undergo endocytosis and partial dephosphorylation during endosomal trafficking, which turn into nanofibres that serve as matrices of intercellular hydrogels on exocytosis. Using cryogenic electron microscopy (cryo-EM), we determined the atomic structures of the D-peptide nanofibres responsible for intercellular gelation. The peptide nanofibres and fibronectin probably interact in secretory

[1]Department of Chemistry, Brandeis University, Waltham, MA, USA. [2]Department of Biochemistry and Molecular Genetics, University of Virginia, Charlottesville, VA, USA. [3]Department of Biochemistry and Molecular Genetics, University of Alabama at Birmingham, Birmingham, AL, USA. [4]O'Neal Comprehensive Cancer Center University of Alabama at Birmingham, Birmingham, AL, USA. ✉e-mail: jerrywang@uab.edu; egelman@virginia.edu; bxu@brandeis.edu

https://doi.org/10.1038/s41565-023-01401-7

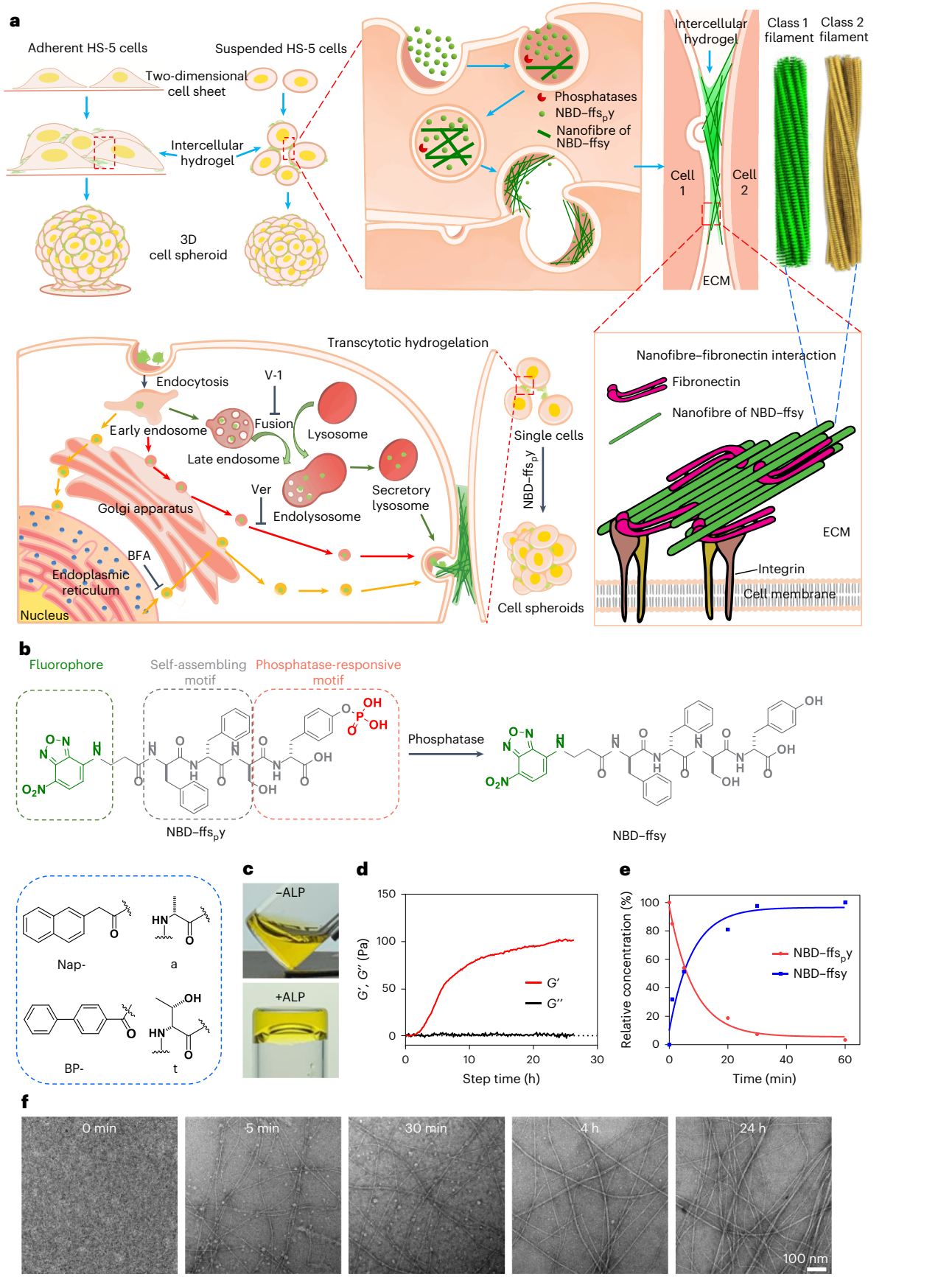

Fig. 1 | Self-assembled D-peptide nanofibres form intercellular hydrogels. **a**, Schematic of the transcytotic dephosphorylation of D-peptide assemblies forming intercellular hydrogels that potentially interact with fibronectin and enable dispersed cells to form cell spheroids. **b**, NBD–ffs$_p$y contains three segments and its reaction in response to phosphatase. **c**, Optical images of NBD–ffs$_p$y (500 μM) in the absence or presence of ALP (0.1 U ml^{-1}) for 24 h in PBS. **d**, Time-dependent strain sweep of NBD–ffs$_p$y (500 μM) with ALP (0.1 U ml^{-1}) addition. **e**, Enzymatic conversion of NBD–ffs$_p$y (500 μM) in the presence of 1 U ml^{-1} ALP in PBS. **f**, TEM images of NBD–ffs$_p$y (500 μM) with ALP (1 U ml^{-1}) addition at designated time points.

https://doi.org/10.1038/s41565-023-01401-7

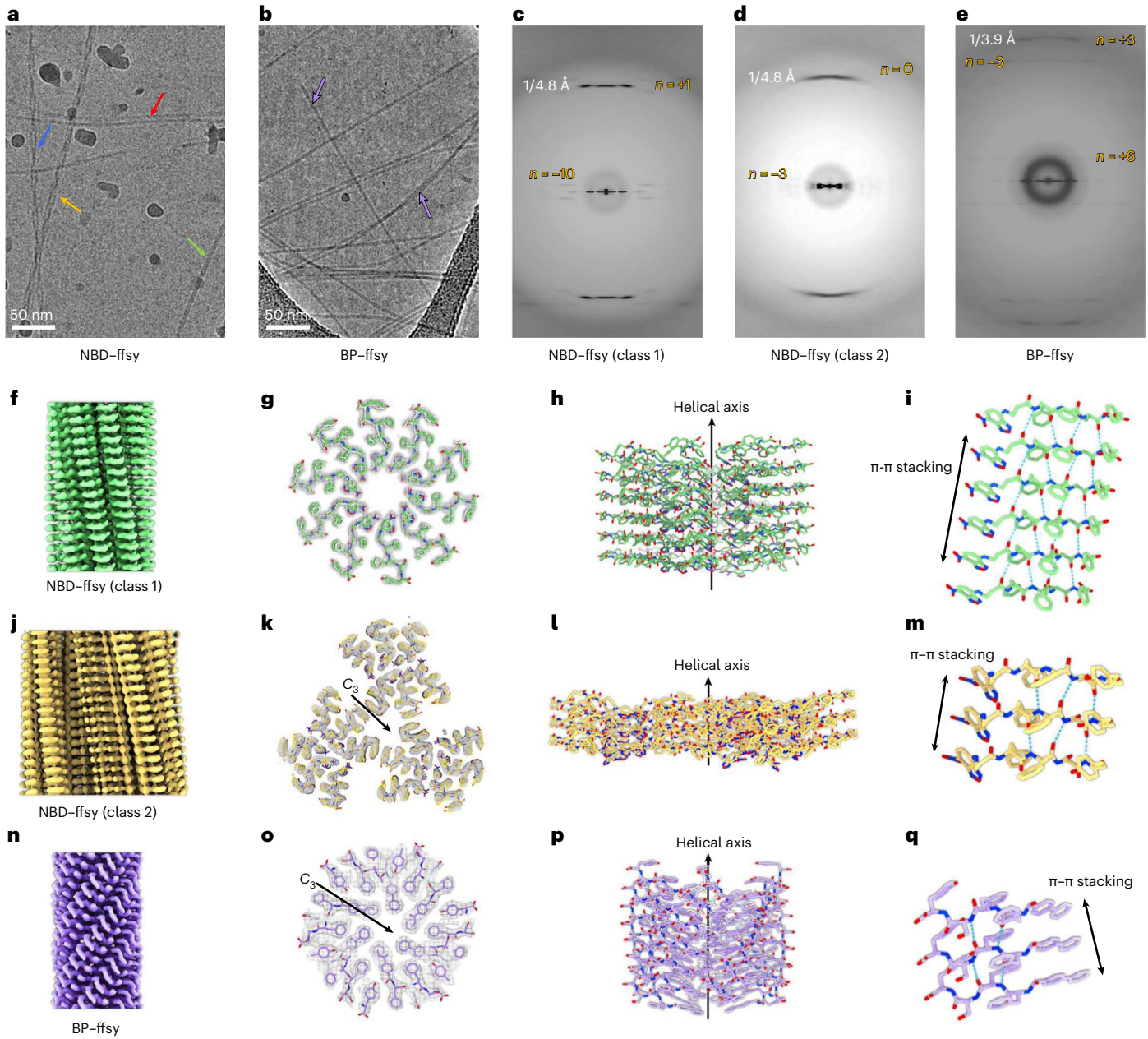

Fig. 2 | NBD–ffsy and BP–ffsy self-assemble into cross-β filaments in vitro. **a**, Cryo-EM image of four types of filament formed by treating NBD–ffs$_p$y (500 μM) with ALP (1 U ml^{-1}) for 24 h. Green arrow, class 1; yellow arrow, class 2; blue arrow, class 3; red arrow, class 4. **b**, Cryo-EM image of filaments formed by treating BP–ffs$_p$y (500 μM) with ALP (0.1 U ml^{-1}) for 24 h. **c**–**e**, Average power spectra of NBD–ffsy class 1 (**c**), NBD–ffsy class 2 (**d**) and BP–ffsy (**e**) filaments. **f**–**h**, Three-dimensional reconstruction (**f**), cross section (**g**) and side view (**h**) of NBD–ffsy class 1 filaments. The black arrow represents the helical axis. **i**, Representation of an array of NBD–ffsy molecules along the axis in class 1 filaments. The dashed lines represent hydrogen bonding. **j**–**l**, Three-dimensional reconstruction (**j**), cross section (**k**) and side view (**l**) of NBD–ffsy class 2 filaments. **m**, Representation of an array of NBD–ffsy molecules along the axis in class 2 filaments. **n**–**p**, Three-dimensional reconstruction (**n**), cross section (**o**) and side view (**p**) of BP–ffsy filaments. **q**, Representation of an array of BP–ffsy molecules along the axis.

vesicles to enable spheroid formation. Minimizing endocytosis, blocking exocytosis, removing phosphate triggers or eliminating nanoparticle-to-nanofibre transformation of the peptide assemblies abolishes cell spheroid formation. Using protease-resistant, enzyme-responsive peptides to mimic ECM biogenesis by generating helical nanofibres as intercellular gelation/matrices for ECM remodelling, this work illustrates a versatile approach that integrates transcytosis with the enzymatic morphological transformation of peptide assemblies for potential applications in regenerative medicine and tissue engineering.

Design of the peptide building block

Figure 1b shows the molecular structures of D-phosphopeptide, which contains fluorescent nitrobenzoxadiazole (NBD) and a self-assembling D-phenylalanine-D-phenylalanine (ff) (refs. 32,33). NBD reports peptide assembly formation in cell assays, as reported previously[34]. As serine and tyrosine are often enriched in the extracellular domain of integral membrane proteins, such as occludin for intercellular adhesion[35], we connected D-serine (s) and D-phosphotyrosine ($_p$y) at the C terminus of ff. Phosphotyrosine endows the D-peptides with phosphatase responsiveness. This design leads to the key molecule,

NBD–ffs$_p$y (**1**). We also examined NBD–ffs$_p$y analogues with similar designs (Supplementary Fig. 1a). According to the cryo-EM structures of the nanofibres of NBD–ffsy (vide infra), biphenyl-4-carboxylic acid (BP) or 2-naphthaleneacetic acid (Nap) replaces NBD to generate BP–ffs$_p$y (**2**) or Nap–ffs$_p$y (**3**), respectively. Since claudin-1, another intercellular junction protein, has an increased extracellular proportion of serines and threonines[36], we doubled the number of D-serines or replaced D-serine with D-threonine (t) for making Nap–ffss$_p$y (**4**) and NBD–fft$_p$y (**5**), respectively, to examine the role of serine or threonine bias for inducing spheroids. Also, L-serine substitutes D-serine to form NBD–ffS$_p$y (**6**) for examining the role of peptide configuration in inducing cell spheroids. Non-bulky D-alanine-D-alanine (aa) replaces ff to generate NBD–aas$_p$y (**7**) for verifying the importance of the ff motif. Switching the position of s and $_p$y generates a scrambled control, NBD–ff$_p$ys (**8**), for examining sequence specificity. NBD–ffsy (**9**) is used for determining the importance of enzymatic dephosphorylation. We used solid-phase peptide synthesis to produce these molecules (Supplementary Fig. 1b) and confirmed their identities using liquid chromatography–mass spectrometry (Supplementary Figs. 9–17).

Enzymatic gelation and self-assembly of NBD–ffs$_p$y

Treating NBD–ffs$_p$y (above its critical micelle concentration (Supplementary Fig. 2)) with alkaline phosphatase (ALP) leads to a hydrogel (Fig. 1c). Strain sweep reveals ALP-instructed fast hydrogelation around 1.5 h, and confirms NBD–ffsy assemblies acting as gel matrices (Fig. 1d and Supplementary Fig. 3), agreeing with ALP rapidly converting NBD–ffs$_p$y to NBD–ffsy (Fig. 1e). Transmission electron microscopy (TEM) images of NBD–ffs$_p$y at designated time points with ALP addition show that fibrils or other higher-order structures are absent before adding ALP. After introducing ALP, NBD–ffs$_p$y self-assembles into nanofibres and eventually forms entangling networks after 24 h (Fig. 1f). The bundle diameter gradually increases and becomes more dispersed over time (Supplementary Fig. 4), agreeing that the NBD–ffsy assemblies are polymorphic (vide infra).

Cryo-EM structures of NBD–ffsy or BP–ffsy fibres

Cryo-EM imaging and reference-free two-dimensional classifications of NBD–ffsy (formed by incubating NBD–ffs$_p$y with ALP for 24 h) confirms polymorphic cross-β filaments (Fig. 2a) with four distinct species accounting for ~36%, 30%, 18% and 16% of the total filaments (Supplementary Fig. 5). Such polymorphisms are observed in almost all the amyloid structures[37–41], such as KFE8 (ref. 42). We tested all the possible symmetries indexed from the averaged power spectrum (Fig. 2c,d) by trial-and-error attempts until recognizable peptide-like features were found in each species. The most dominant filament species (class 1) has a helical rise of 0.48 Å and twist of 35.8°, with a resolution of ~3.10 Å estimated by Fourier shell correlation (FSC) (Supplementary Fig. 6). The filament reconstruction shows parallel cross-β packing of the NBD–ffsy molecules, with the heteroaromatic NBD pointing towards the centre and the hydrophilic serine–tyrosine pointing outwards of the filaments (Fig. 2f,g). The filaments are held together by extensive β-sheet hydrogen bonding and aromatic–aromatic stacking interactions between NBD and D-phenylalanine (Fig. 2h,i). Three-dimensional (3D) reconstruction of class 2 filaments reached ~3.2 Å resolution with a helical rise of 4.8 Å and twist of −1.7°. The filament model possesses C_3 symmetry, and each asymmetrical unit contains six copies of NBD–ffsy (Fig. 2j,k). The cross-β packing of class 2 filaments depends on the hydrogen bonding between amides and π–π stacking among NBD motifs, displaying the carboxylic acid and hydroxyl group from tyrosine (Fig. 2l,m). The polymorphic assemblies of NBD–ffsy include two other species with distinct molecular packings (Supplementary Fig. 7). Although density appears at the C_3 axis, the limited resolution of imaging prevents the unambiguous assignment of atomistic structures to the density maps of class 3 and 4 filaments.

BP–ffsy, on the other hand, forms homogeneous filaments that reach ~2.6 Å resolution (Supplementary Fig. 8). Based on the averaged power spectrum (Fig. 2e), a 3D reconstruction of the filaments shows that the hydrophobic biphenyl motifs arrange at the centre with C_3 symmetry, a helical rise of 2.11 Å and twist of −54.8° (Fig. 2n,o). Unlike NBD–ffsy, the tyrosines in the BP–ffsy filaments point inwards, and display C-terminal carboxylic acid and hydroxyl groups from serines (Fig. 2p). BP–ffsy filaments also display cross-β packing and π–π stacking among biphenyl motifs (Fig. 2q). Similarly, all the three types of filament display C-terminal carboxylic acid and hydroxyl groups on the surface, which may account for their spheroid-inducing property (vide infra).

Intercellular hydrogels for cell spheroid formation

HS-5 cells can serve as a reliable assay for examining the morphogenic effects of the D-peptide assemblies because they remain as single-layer individual cells under normal culture conditions, and hardly form cell clumps when overconfluent. At non-toxic concentrations (≤500 μM; Supplementary Fig. 18), NBD–ffs$_p$y leads to spheroids in both adherent and suspended HS-5 cells (Fig. 3a,b), with the extracellular distribution of assemblies within spheroids (indicated by the white arrow). In particular, NBD–ffs$_p$y quickly induces aggregation in suspended cells within 12 h. The spheroid sizes positively correlate with the concentrations (Supplementary Fig. 19a,b) and negatively correlate with poly-D-lysine dish coating (Supplementary Fig. 19c), suggesting that NBD–ffs$_p$y promotes cell–cell adhesion over cell–substrate adhesion. The spheroids gradually dissociate in fresh media, with the disappearance of intercellular fluorescence (Fig. 3c) and fusion of some of the neighbouring spheroids during dissociation (Supplementary Fig. 20). The reversible cell aggregation agrees with the dynamic non-covalent interactions among the D-peptides, which 'glue' the HS-5 cells together. Nuclei and live-/dead-cell staining confirms 3D cell aggregate formation (Fig. 3d,e), accompanied by a necrotic core and a gradual decrease in viable cells from the periphery to the centre of the spheroids (Fig. 3f

Fig. 3 | Spheroids from adherent and suspended HS-5 cells consist of intercellular hydrogel that colocalizes with fibronectin. a, Differential interference contrast imaging and fluorescence 3D reconstruction of adherent HS-5 cells treated with NBD–ffs$_p$y (500 μM) for 24 h. **b**, Confocal images of suspended HS-5 cells treated with NBD–ffs$_p$y (300 μM) for 48 h. The white arrow points to assemblies within the spheroids. **c**, Phase contrast and confocal images of HS-5 cell spheroid disassembles in a fresh medium within 72 h. **d**, *Z*-axis projection of nuclei and live-/dead-cell staining of the spheroids formed by treating suspended HS-5 cells with BP–ffs$_p$y (50 μM) for 72 h. **e**, Three-dimensional rendering of the live-/dead-cell staining of the spheroid in **d**. **f**, Spatial intensity profiles from the area indicated by the arrow in **d**. **g**, Hypoxia staining of HS-5 cell spheroids formed by treating with BP–ffs$_p$y (50 μM) for 72 h. **h**, Spatial intensity profiles from the area indicated by the arrow in **g**. **i**, F-actin staining of HS-5 spheroids formed by treating with BP–ffs$_p$y (50 μM) for 72 h. **j**, Representative confocal images of the FRAP assay on suspended HS-5 cells incubated with NBD–ffs$_p$y (200 μM) for 48 h. **k**, Quantitative analysis of the fluorescence intensity of the FRAP assay in **j**. **l**, Confocal images of the aggregation of suspended HS-5 cells in the presence of NBD–ffs$_p$y (500 μM) within 6 h. **m**, Zoomed-in images of the NBD channel of HS-5 cells at designated time points. The white arrows indicate pericellular assemblies. **n**,**o**, Immunofluorescence staining (**n**) and corresponding colocalization scatter plots (**o**) of adherent HS-5 cells treated with NBD–ffs$_p$y (500 μM) for 72 h and then fixed and stained with antibodies. **p**, Manders' correlation coefficients of the fluorescence from NBD (green) and fluorescence from the target protein (magenta). M1, fraction of green overlapping with magenta; M2, fraction of magenta overlapping with green. Data are presented as mean ± s.d. ($n = 3$ independent measurements).

https://doi.org/10.1038/s41565-023-01401-7

and Supplementary Fig. 21). Hypoxia staining suggests a hypoxic core (Fig. 3g,h). F-actin staining displays a cytoskeleton rearrangement with oriented distribution at the periphery, indicating spheroid compaction (Fig. 3i). Cadherin staining reveals the cell–cell junctions, which are more evident in E-cadherin-abundant MCF-7 spheroids (Supplementary Fig. 22). Liquid chromatography–mass spectrometry analysis shows

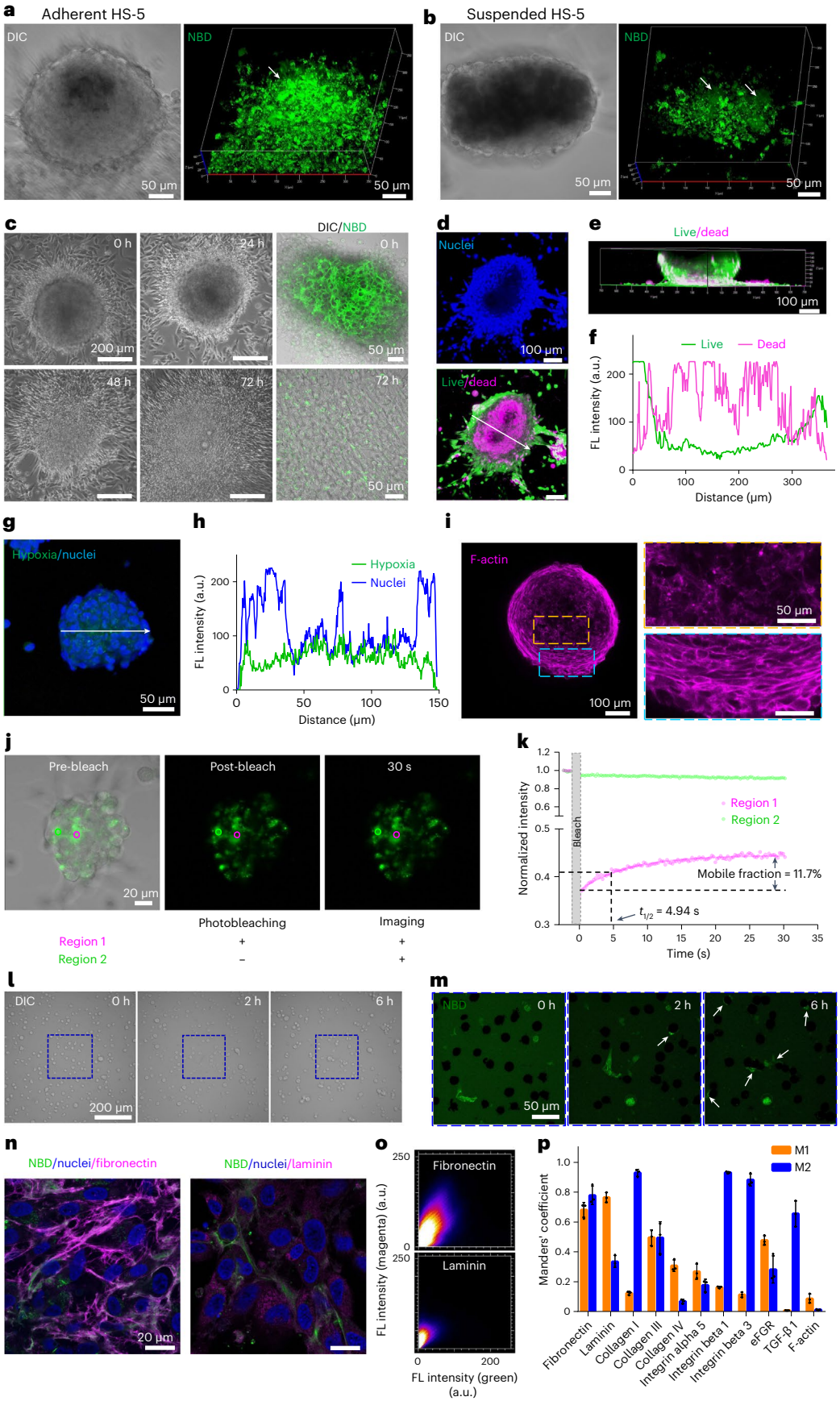

https://doi.org/10.1038/s41565-023-01401-7

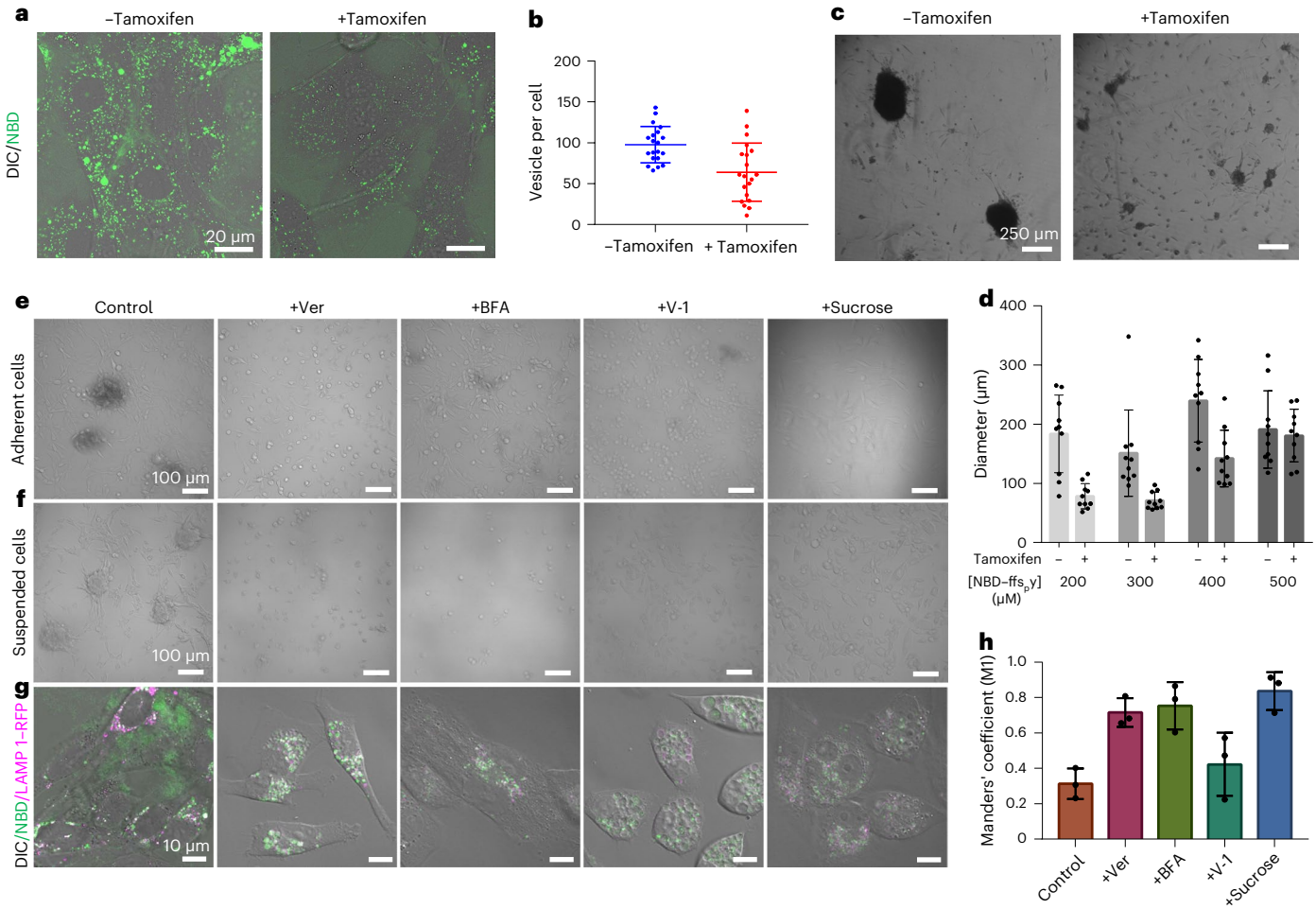

Fig. 4 | Endocytosis and exocytosis are crucial for spheroid formation. **a**, Confocal images of TKO cells with or without tamoxifen treatment incubated with NBD–ffs$_p$y (200 μM) for 1 h. **b**, Number of vesicles per cell in **a**. Data are presented as mean ± s.d. (n = 20 cells per group). **c**, Suspended TKO cells with or without tamoxifen incubated with NBD–ffs$_p$y (200 μM) for 48 h. **d**, Diameters of the TKO spheroids with or without tamoxifen treatment induced by NBD–ffs$_p$y (200–500 μM). Data are presented as mean ± s.d. (n = 10 spheroids per group). **e**, Confocal images of adherent HS-5 cells with NBD–ffs$_p$y (500 μM) under different treatments for 48 h. Control (NBD–ffs$_p$y), +Ver (NBD–ffs$_p$y + 20 μM Ver), +BFA (NBD–ffs$_p$y + 50 nM BFA), +V-1 (NBD–ffs$_p$y + 10 μM V-1) and sucrose (NBD–ffs$_p$y). **f**, Confocal images of suspended HS-5 cells under different treatments for 48 h (NBD–ffs$_p$y at 200 μM due to removed cell–substrate adhesion). Control (NBD–ffs$_p$y), +Ver (NBD–ffs$_p$y + 50 μM Ver), +BFA (NBD–ffs$_p$y + 300 nM BFA), +V-1 (NBD–ffs$_p$y + 10 μM V-1) and sucrose (NBD–ffs$_p$y). **g**, Confocal images of LAMP1–RFP-labelled HS-5 cells incubated under the same condition as the cells in **e**. Sucrose-pretreated cells: HS-5 cells preincubated with 0.1 M sucrose for 72 h. **h**, Manders' correlation coefficients of the green and magenta fluorescence from cells in **g**. M1, fraction of green overlapping with magenta. Data are presented as mean ± s.d. (n = 3 independent measurements).

20% NBD–ffs$_p$y and 80% NBD–ffsy in the assemblies (Supplementary Fig 23) from the spheroids. Their mixture at this ratio forms nanofibres in PBS (Supplementary Fig. 24).

Fluorescence recovery after photobleaching (FRAP) shows that the intercellular fluorescence hardly recovers after photobleaching (Fig. 3j), with a mobile fraction of 11.7% and a half-time of recovery ($t_{1/2}$) of 4.94 s (Fig. 3k), suggesting poor diffusivity. Coincubating cells with NBD–ffs$_p$y and diffusive small-molecule probes (rhodamine B or Nile red) displays trapped probes with poor recovery (Supplementary Figs. 25 and 26), indicating intercellular hydrogelation. Differential interference contrast images show scattered cells at 0 h and cell aggregates after 6 h (Fig. 3l). The individual cells show random motion within 0–3 h and become 'sticky' and undergo gradual aggregation from 3 to 6 h (Supplementary Video 1). The NBD channel displays peri-/intercellular D-peptide assemblies (indicated by white arrows) from 2 to 6 h, which occurs simultaneously with morphogenesis (Fig. 3m). The immunofluorescence staining of various ECM proteins, surface receptors and cytoskeleton on NBD–ffs$_p$y-treated HS-5 cells shows that the peptide assemblies colocalize with several ECM proteins (Fig. 3n,o and Supplementary Fig. 27), especially with fibronectin that has sufficient signal intensities to achieve good colocalization for both M1 (fraction of NBD overlapping with protein) and M2 (fraction of protein overlapping with NBD) (Fig. 3p). Collectively, these results indicate that NBD–ffs$_p$y undergoes dephosphorylation to form intercellular hydrogels that colocalize with fibronectin to promote cell–cell adhesion and generate spheroids.

BP–ffs$_p$y allows enzymatic dephosphorylation and enhances the self-assembling ability to form nanofibres at low concentrations. BP–ffs$_p$y induces large spheroids with a tenfold decrease in its effective concentrations (25–100 μM) (Supplementary Fig. 28a–d). The spheroids induced by BP–ffs$_p$y trap small-molecule probes (Supplementary Fig. 28e,f), suggesting in situ hydrogelation. Nap–ffs$_p$y, Nap–ffss$_p$y and NBD–fft$_p$y display similar morphologies of nanofibres after dephosphorylation (Supplementary Fig. 29c) and induce HS-5 cell spheroid formation (Supplementary Fig. 29a,b). NBD–ff$_p$ys only induces small spheroids in suspended cells at high concentrations, which correlates

with the fact that NBD–ffys is a weak hydrogelator (Supplementary Fig. 29d). NBD–aas$_p$y or NBD–ffs$_p$y abolishes the nanoparticle-to-nanofibre morphological transformation on ALP addition. Neither of them induces cell spheroids (Supplementary Fig. 29a,b). Preassembled NBD–ffsy nanofibres, forming chunks of hydrogels deposited on the cell surface, fail to induce spheroids (Supplementary Figs. 29e and 30). Mixing NBD–ffs$_p$y with NBD–ffsy generates preassembled fibrils and hydrogel chunks that undermines the spheroid-inducing ability (Supplementary Fig. 31). These results suggest the crucial role of morphological transformation and in situ hydrogelation for cell spheroid formation.

Transcytosis of D-peptide assemblies

Inspired by the synthesis of cellular fibronectin that involves the secretion of soluble protein dimers and subsequent self-assembly into an insoluble matrix[43], we examined the roles of transcytosis in spheroid formation. We first used endocytosis inhibitors of distinct pathways and found that chlorpromazine, a clathrin-mediated endocytosis inhibitor, considerably reduces the cellular uptake of NBD–ffs$_p$y (Supplementary Fig. 32). Due to the toxicity of chlorpromazine to HS-5 cells (Supplementary Fig. 33a), we turned to tamoxifen-induced dynamin triple knockout (TKO) mouse fibroblast to reduce endocytosis. After the verification of successful knockout (~90%) (Supplementary Fig. 34a,b), confocal images show a reduced number of vesicles per cell accompanied with decreased sizes of spheroids, suggesting the crucial role of endocytosis in spheroid formation (Fig. 4a–d and Supplementary Fig. 34c).

We used three types of exocytosis inhibitor to inhibit secretion: (1) verapamil (Ver) for inhibiting calcium-dependent exocytosis; (2) brefeldin A (BFA) for inhibiting conventional endosomal trafficking; (3) vacuolin-1 (V-1) and sucrose for inducing vacuolation, with V-1 preventing unconventional endolysosomal secretion[44]. Treating HS-5 cells at non-toxic concentrations (Supplementary Fig. 33b–d), all the three inhibitors undermine spheroid formation in both adherent and suspended HS-5 cells (Fig. 4e,f). Moreover, the exocytosis inhibitors abolish spheroid formation in a previously reported spheroid-inducing D-peptide, Nap–ffk(biotin)$_p$y (Supplementary Fig. 35), demonstrating the generality of this exocytotic mechanism in generating spheroids. Unlike the uninhibited cells that display extracellular assemblies, inhibitor-treated groups exhibit a reversible intracellular distribution of NBD–ffs$_p$y puncta, suggesting the endosomal localization of D-peptides (Supplementary Fig. 36). NBD colocalizes with LAMP1–RFP after Ver, BFA or sucrose treatment, whereas uninhibited cells display less colocalization, further supporting the NBD–ffs$_p$y endosomal localization. V-1 induces vacuolation and prevents endosome–lysosome fusion, which results in poor colocalization, too (Fig. 4g,h and Supplementary Fig. 37). These results support the fact that NBD–ffs$_p$y induces spheroids by the transcytosis of D-peptide filaments into the intercellular space.

To determine whether dephosphorylation happens extracellularly by ecto-phosphatases or intracellularly during endosomal trafficking, we added ALP to the culture media. Extracellular ALP addition reduces intercellular assemblies and cell aggregation, unless diluting ALP to ultralow levels (for example, 0.001 U ml^{-1}) (Fig. 5a and Supplementary 38). Moreover, inhibiting tissue-non-specific ALP (TNAP) overexpressed by SJSA-1 cells increases the sizes of spheroids for SJSA-1 treated by NBD–ffs$_p$y or BP–ffs$_p$y (Fig. 5b,c). TNAP inhibition results in the colocalization of peptide fibres with fibronectin, but the fibres form throughout the cells and poorly localize with fibronectin in uninhibited SJSA-1 (Fig. 5d,e). These results support that NBD–ffs$_p$y mainly undergoes intracellular dephosphorylation during endosomal trafficking to generate intercellular assemblies and indicate that extracellular dephosphorylation disfavour fibronectin colocalization to hamper spheroid formation.

We incubated NBD–ffs$_p$y with nine additional cell lines expressing different levels of phosphatases for evaluating the generality. Enzymatic dephosphorylation of NBD–ffs$_p$y by cells displays fast conversion in Saos-2, SJSA-1 and HeLa, accompanied with the membrane deposition of assemblies and decreased cell viability (Supplementary Fig. 39), similar to the previous results[45,46]. Spheroid sizes differ among the cell lines. HS-5 and U-87MG cells form large spheroids, whereas PC-3, MCF-7, OVSAHO, SKOV-3, HepG2 and SJSA-1 cells form smaller ones. HeLa and Saos-2 cells hardly form cell aggregates. U-87 MG spheroids grow over time, like HS-5, in a concentration-dependent manner (Fig. 5f,g and Supplementary Figs. 39b,c and 40a).

Immunostaining shows cell-type-specific morphologies of fibronectin, with HS-5, SJSA-1 and U-87 MG mainly display fibrillar fibronectin, whereas SKOV-3, MCF-7 and HepG2 show globular fibronectin. HeLa, OVSAHO, Saos-2 and PC-3 display a weak signal. These results correspond to the tissue-dependent isoforms of fibronectin, such as soluble plasma fibronectin by hepatocytes and insoluble cellular fibronectin by fibroblasts[43]. NBD–ffs$_p$y is more potent among cells expressing fibrillar fibronectin and low phosphatase levels (Fig. 5h and Supplementary Fig. 40b–d). BP–ffs$_p$y induces spheroids of SJSA-1 and SKOV-3, with the formation of a necrotic core (Supplementary Fig. 41). We also coincubated HS-5 with other cell lines to introduce fibrillar fibronectin and mimic the tumour microenvironment. BP–ffs$_p$y induces heterotypic spheroids in HS-5 with PC-3–DsRed, Saos-2–GFP, SJSA-1–RFP or HeLa–GFP, with the fluorescent cancer cells distributing throughout the spheroids (Supplementary Fig. 42). These results support the crucial role of fibrillar fibronectin in spheroid formation.

D-peptide nanofibres facilitate fibronectin fibrillogenesis

We conducted the live-cell imaging of HS-5 cells incubated with rhodamine–fibronectin (rFN) and NBD–ffs$_p$y. HS-5 quickly processes the rFN derived from plasma to form fibrillar structures, whereas NBD–ffs$_p$y undergoes punctum-to-fibril transformation and gradual colocalization with rFN (Fig. 6a). The sizes of rFN increases as it colocalizes with NBD–ffs$_p$y in 24–72 h, indicating NBD–ffs$_p$y-facilitated fibronectin remodelling. NBD–ffs$_p$y and rFN exhibit an early partial overlap in endosomes in 4 h, followed by the initiation of intercellular colocalization in 24 h, which gradually achieved good overlay in 48–72 h (Fig. 6b–d). Under the cell-free condition, incubating rFN with ALP or NBD–ffs$_p$y retains the globular structure, whereas coincubation with nanofibres of NBD–ffsy, either preassembled (NBD–ffsy) or enzymatically formed (NBD–ffs$_p$y + ALP), facilitates the fibrillogenesis of rFN (Fig. 6e). NBD–ffs$_p$y-induced crowding probably promotes rFN aggregates, which transform into radiating nanofibres from aggregates on ALP addition. Reducing the initial NBD–ffs$_p$y concentrations decreases the sizes of aggregates (Supplementary Fig. 43). Colocalization analysis reveals rFN with background fluorescence from NBD–ffs$_p$y in the absence of ALP (Fig. 6f), whereas incubating with NBD nanofibres increases colocalization (Fig. 6g,h). The enzymatic nanofibres are invisible under confocal microscopy, suggesting finite and homogeneous nanostructures. Therefore, we pretreated NBD–ffs$_p$y with ALP to generate enzymatic nanofibres, and then incubated with rFN. Confocal images show colocalization with the evident fibrillogenesis of rFN, supporting the ECM remodelling effects of NBD–ffsy nanofibres (Fig. 6i–k). The more potent spheroid-inducing analogue, BP–ffs$_p$y, when pretreated with ALP to form enzymatic nanofibres, induces curly fibres of rFN that entangle into 3D networks (Fig. 6l,m). The fibrillogenic concentrations correspond to the spheroid-inducing concentrations, where high concentrations of BP–ffs$_p$y lead to large chunks of rFN fibrils and fail to induce spheroids (Fig. 6n and Supplementary Fig. 28d).

We used TEM to image NBD–ffs$_p$y with rFN in the presence of ALP. Although 100 μM of NBD–ffs$_p$y results in amorphous aggregates, wider nanofibres (indicated by red arrows) with helical features (Fig. 6o) appear at 400 μM of NBD–ffs$_p$y. Starting from 50 μM of BP–ffs$_p$y treated with ALP, the TEM images show close-packed bundles of nanofibres with 50 or 25 μg ml^{-1} of fibronectin. Decreasing to 5 μg ml^{-1}

https://doi.org/10.1038/s41565-023-01401-7

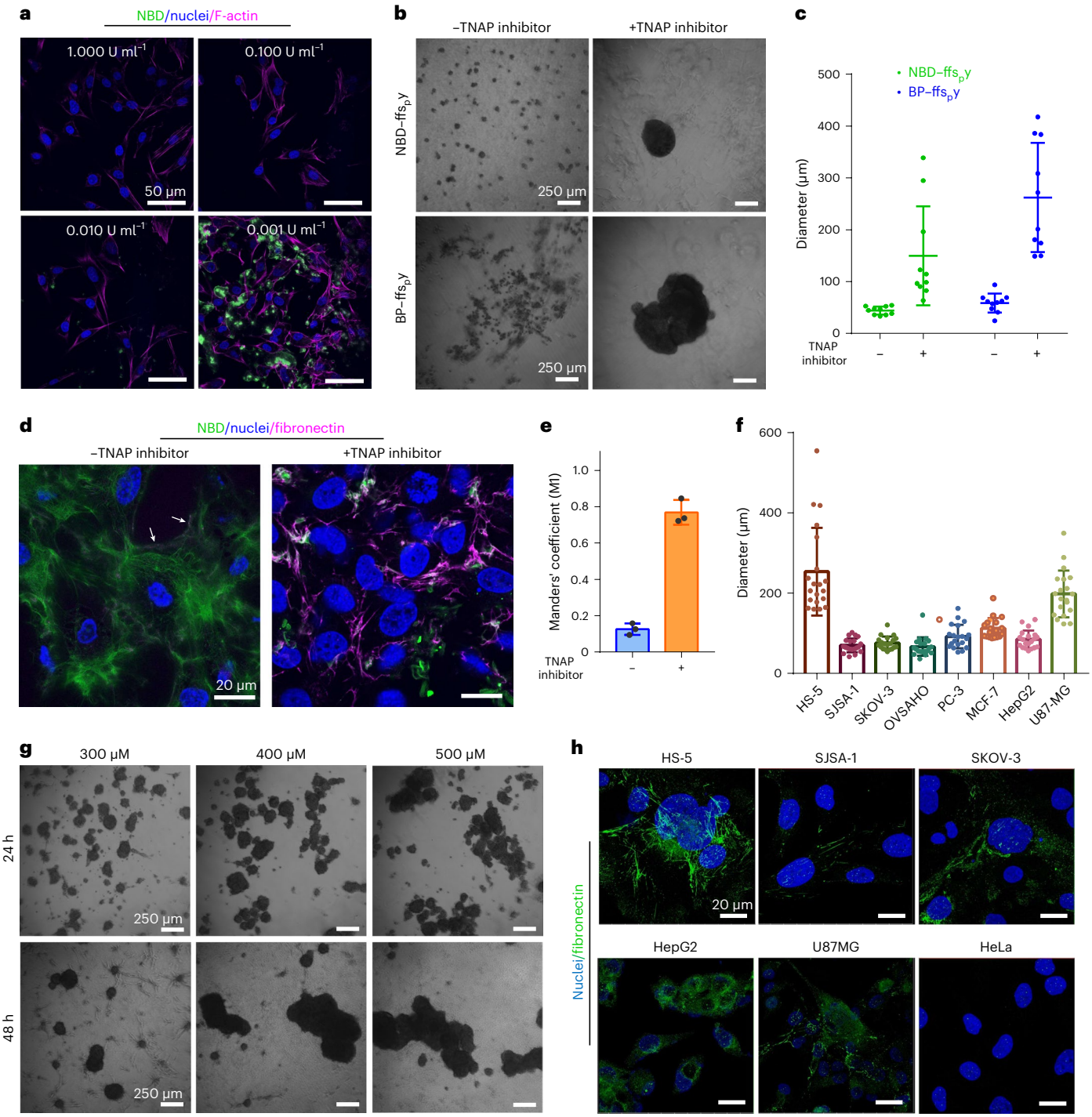

Fig. 5 | Intracellular dephosphorylation is crucial for spheroid formation. **a**, Confocal images of adherent HS-5 cells treated with NBD–ffs$_p$y (400 μM) in serum-free DMEM medium for 24 h with different concentrations of ALP addition. **b**, Phase-contrast images of suspended SJSA-1 cells incubated with NBD–ffs$_p$y (400 μM) or BP–ffs$_p$y (100 μM) in the presence or absence of TNAP inhibitor (5 μM) for 48 h. **c**, Diameters of SJSA-1 spheroids in **b**. Data are presented as mean ± s.d. (n = 10 spheroids per group). **d**, Immunofluorescence staining of adherent SJSA-1 cells treated with NBD–ffs$_p$y (500 μM) in the presence or absence of TNAP inhibitor (5 μM) for 72 h. The white arrows indicate fibronectin. **e**, Manders' correlation coefficients of the green and magenta fluorescence from cells in **d**. M1, fraction of green overlapping with magenta. Data are presented as mean ± s.d. (n = 3 independent measurements). **f**, Quantification of the sizes of the spheroids formed by treating suspended cells with NBD–ffs$_p$y (500 μM) for 48 h. Data are presented as mean ± s.d. (n = 20 spheroids per group). **g**, Phase-contrast images of suspended U-87 MG cells in the treatment of NBD–ffs$_p$y (300–500 μM) for 24 or 48 h. **h**, Z-axis projections of immunofluorescence staining of fibronectin in various cell lines.

of fibronectin leads to loose-packed nanofibres with aggregates in between (Fig. 6p). The fibronectin-dependent morphology indicates the potential interactions of the peptide assemblies with fibronectin.

Conclusion

In brief, we examined the structures and mechanism of D-peptide nanofibres formed within the intercellular space of HS-5 cells, which

https://doi.org/10.1038/s41565-023-01401-7

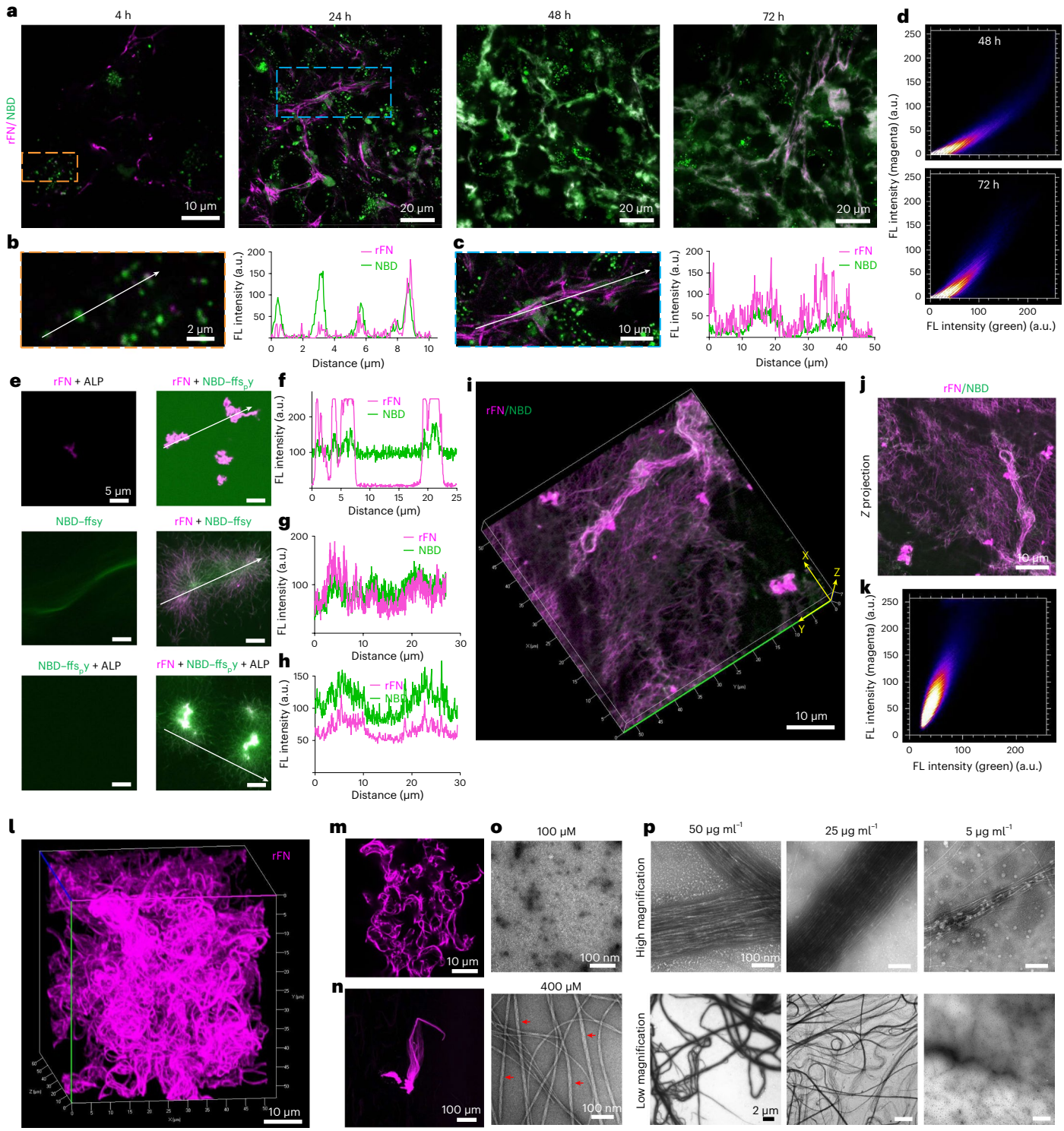

Fig. 6 | D-peptide nanofibres facilitate the fibrillogenesis of fibronectin. **a**, Confocal images of adherent HS-5 cells treated with rFN (5 μg ml^{-1}) and NBD–ffs$_p$y at various time points. **b**,**c**, Spatial intensity profiles of HS-5 cells in the magnified area in **a** incubated for 4 h (**b**) or 24 h (**c**). **d**, Colocalization scatter plots of the fluorescence intensities from cells in **a** incubated for 48 or 72 h. **e**, Confocal images of samples incubated at 37 °C for 24 h: rFN + ALP (top left); NBD–ffsy (middle left); NBD–ffs$_p$y + ALP (bottom left); rFN + NBD–ffs$_p$y (top right); rFN + NBD–ffsy (middle right); rFN + NBD–ffs$_p$y + ALP (bottom right). **f**–**h**, Spatial intensity profiles of rFN + NBD–ffs$_p$y (**f**), rFN + NBD–ffsy (**g**) or rFN + NBD–ffs$_p$y + ALP (**h**) in **e**. **i**, Three-dimensional rendering of NBD–ffs$_p$y treated with ALP for 48 h and then incubated with rFN for 9 h. **j**, *Z*-axis projection of the stack in **i**. **k**, Colocalization scatter plot of fluorescence intensities form two channels in **j**. **l**, Three-dimensional rendering of BP–ffs$_p$y treated with ALP for 48 h and then incubated with rFN for 24 h. **m**, One slice of the confocal image from **l**. **n**, *Z*-axis projection of BP–ffs$_p$y (500 μM) treated with ALP for 48 h and then incubated with rFN for 24 h. **o**, TEM images of rFN incubated with NBD–ffs$_p$y (100 or 400 μM) in the presence of ALP for 48 h. The red arrows indicate nanofibres with increased diameters. **p**, TEM images of BP–ffs$_p$y treated with ALP for 48 h and then incubated with fibronectin (50, 25 or 5 μg ml^{-1}). [rFN] = 50 μg ml^{-1}, [NBD–ffsy] = 500 μM, [NBD–ffs$_p$y] = 500 μM, [BP–ffs$_p$y] = 50 μM and [ALP] = 0.1 U ml^{-1}, unless indicated otherwise.

quickly form spheroids in both adherent and suspended conditions. Our findings showed that the self-assembling motif, phosphate and nanoparticle-to-nanofibre transformation are indispensable for spheroid formation. Having a phosphotyrosine residue, NBD–ffs$_p$y undergoes transcytotic dephosphorylation to create intercellular assemblies that colocalize with fibronectin. These peptide assemblies facilitate the fibrillogenesis of fibronectin and act as reversible intercellular nanojunctions that glue cells together. By forming an adaptive supramolecular hydrogel[47] that remodels endogenous proteins and controls reaction–diffusion at the nano- and microscale[48,49], this work illustrates the potential of integrating cryo-EM, enzymatic shapeshifting (nanoparticle to nanofibres) and cell biology (endocytosis and exocytosis) to mimic ECM biogenesis. Based on the phenotype switch in the differentiation of stem cells[50], the approach taken in this work should be useful for guiding cell differentiation, which is the subject of an ongoing study.

Online content

Any methods, additional references, Nature Portfolio reporting summaries, source data, extended data, supplementary information, acknowledgements, peer review information; details of author contributions and competing interests; and statements of data and code availability are available at https://doi.org/10.1038/s41565-023-01401-7.

References

1. Rookmaaker, M. B., Schutgens, F., Verhaar, M. C. & Clevers, H. Development and application of human adult stem or progenitor cell organoids. *Nat. Rev. Nephrol.* **11**, 546–554 (2015).
2. Baharvand, H., Hashemi, S. M., Kazemi Ashtiani, S. & Farrokhi, A. Differentiation of human embryonic stem cells into hepatocytes in 2D and 3D culture systems in vitro. *Int. J. Dev. Biol.* **50**, 645–652 (2006).
3. Benya, P. D. & Shaffer, J. D. Dedifferentiated chondrocytes reexpress the differentiated collagen phenotype when cultured in agarose gels. *Cell* **30**, 215–224 (1982).
4. Nelson, C. M. & Bissell, M. J. Modeling dynamic reciprocity: engineering three-dimensional culture models of breast architecture, function, and neoplastic transformation. *Semin. Cancer Biol.* **15**, 342–352 (2005).
5. Imamura, Y. et al. Comparison of 2D- and 3D-culture models as drug-testing platforms in breast cancer. *Oncol. Rep.* **33**, 1837–1843 (2015).
6. Weaver, V. M. et al. Reversion of the malignant phenotype of human breast cells in three-dimensional culture and in vivo by integrin blocking antibodies. *J. Cell Biol.* **137**, 231–245 (1997).
7. Bhadriraju, K. & Chen, C. S. Engineering cellular microenvironments to improve cell-based drug testing. *Drug Discov. Today* **7**, 612–620 (2002).
8. Yamada, K. M. & Cukierman, E. Modeling tissue morphogenesis and cancer in 3D. *Cell* **130**, 601–610 (2007).
9. Cukierman, E., Pankov, R., Stevens, D. R. & Yamada, K. M. Taking cell-matrix adhesions to the third dimension. *Science* **294**, 1708–1712 (2001).
10. Gao, D. et al. Organoid cultures derived from patients with advanced prostate cancer. *Cell* **159**, 176–187 (2014).
11. Karthaus, W. R. et al. Identification of multipotent luminal progenitor cells in human prostate organoid cultures. *Cell* **159**, 163–175 (2014).
12. Drost, J. et al. Organoid culture systems for prostate epithelial and cancer tissue. *Nat. Protoc.* **11**, 347–358 (2016).
13. Kelm, J. M., Timmins, N. E., Brown, C. J., Fussenegger, M. & Nielsen, L. K. Method for generation of homogeneous multicellular tumor spheroids applicable to a wide variety of cell types. *Biotechnol. Bioeng.* **83**, 173–180 (2003).
14. Zheng, H. et al. Rotary culture promotes the proliferation of MCF-7 cells encapsulated in three-dimensional collagen–alginate hydrogels via activation of the ERK1/2-MAPK pathway. *Biomed. Mater.* **7**, 015003 (2012).
15. Raghavan, S. et al. Comparative analysis of tumor spheroid generation techniques for differential in vitro drug toxicity. *Oncotarget* **7**, 16948–16961 (2016).
16. Marchi, F. & Leblond, C. P. Collagen biogenesis and assembly into fibrils as shown by ultrastructural and 3H-proline radioautographic studies on the fibroblasts of the rat food pad. *Am. J. Anat.* **168**, 167–197 (1983).
17. McCaffrey, G. et al. Tight junctions contain oligomeric protein assembly critical for maintaining blood–brain barrier integrity in vivo. *J. Neurochem.* **103**, 2540–2555 (2007).
18. Seger, D., Seger, R. & Shaltiel, S. The CK2 phosphorylation of vitronectin. Promotion of cell adhesion via the $\alpha_v\beta_3$-phosphatidylinositol 3-kinase pathway. *J. Biol. Chem.* **276**, 16998–17006 (2001).
19. Weber, G. F. et al. Phosphorylation-dependent interaction of osteopontin with its receptors regulates macrophage migration and activation. *J. Leukoc. Biol.* **72**, 752–761 (2002).
20. Yalak, G. & Vogel, V. Extracellular phosphorylation and phosphorylated proteins: not just curiosities but physiologically important. *Sci. Signal.* **5**, re7 (2012).
21. Wu, D. et al. Polymers with controlled assembly and rigidity made with click-functional peptide bundles. *Nature* **574**, 658–662 (2019).
22. Du, X., Zhou, J., Shi, J. & Xu, B. Supramolecular hydrogelators and hydrogels: from soft matter to molecular biomaterials. *Chem. Rev.* **115**, 13165–13307 (2015).
23. Cheetham, A. G., Zhang, P., Lin, Y. A., Lock, L. L. & Cui, H. Supramolecular nanostructures formed by anticancer drug assembly. *J. Am. Chem. Soc.* **135**, 2907–2910 (2013).
24. Tibbitt, M. W. & Anseth, K. S. Hydrogels as extracellular matrix mimics for 3D cell culture. *Biotechnol. Bioeng.* **103**, 655–663 (2009).
25. Jayawarna, V. et al. Nanostructured hydrogels for three-dimensional cell culture through self-assembly of fluorenylmethoxycarbonyl–dipeptides. *Adv. Mater.* **18**, 611–614 (2006).
26. Smith, D. J. et al. A multiphase transitioning peptide hydrogel for suturing ultrasmall vessels. *Nat. Nanotechnol.* **11**, 95–102 (2016).
27. Alvarez, Z. et al. Bioactive scaffolds with enhanced supramolecular motion promote recovery from spinal cord injury. *Science* **374**, 848–856 (2021).
28. Winkler, S. M., Harrison, M. R. & Messersmith, P. B. Biomaterials in fetal surgery. *Biomater. Sci.* **7**, 3092–3109 (2019).
29. Wang, H., Feng, Z. & Xu, B. Intercellular instructed-assembly mimics protein dynamics to induce cell spheroids. *J. Am. Chem. Soc.* **141**, 7271–7274 (2019).
30. Wang, H. et al. An in situ dynamic continuum of supramolecular phosphoglycopeptides enables formation of 3D cell spheroids. *Angew. Chem. Int. Ed.* **56**, 16297–16301 (2017).
31. He, H. et al. Enzymatic noncovalent synthesis. *Chem. Rev.* **120**, 9994–10078 (2020).
32. Zhang, Y., Kuang, Y., Gao, Y. & Xu, B. Versatile small-molecule motifs for self-assembly in water and the formation of biofunctional supramolecular hydrogels. *Langmuir* **27**, 529–537 (2011).
33. Reches, M. & Gazit, E. Casting metal nanowires within discrete self-assembled peptide nanotubes. *Science* **300**, 625–627 (2003).
34. Gao, Y., Shi, J., Yuan, D. & Xu, B. Imaging enzyme-triggered self-assembly of small molecules inside live cells. *Nat. Commun.* **3**, 1033 (2012).

35. Van Itallie, C. M. & Anderson, J. M. Occludin confers adhesiveness when expressed in fibroblasts. *J. Cell Sci.* **110**, 1113–1121 (1997).
36. Mrsny, R. J. et al. A key claudin extracellular loop domain is critical for epithelial barrier integrity. *Am. J. Pathol.* **172**, 905–915 (2008).
37. Lee, M., Ghosh, U., Thurber, K. R., Kato, M. & Tycko, R. Molecular structure and interactions within amyloid-like fibrils formed by a low-complexity protein sequence from FUS. *Nat. Commun.* **11**, 5735 (2020).
38. Roder, C. et al. Atomic structure of PI3-kinase SH3 amyloid fibrils by cryo-electron microscopy. *Nat. Commun.* **10**, 3754 (2019).
39. Cao, Q., Boyer, D. R., Sawaya, M. R., Ge, P. & Eisenberg, D. S. Cryo-EM structures of four polymorphic TDP-43 amyloid cores. *Nat. Struct. Mol. Biol.* **26**, 619–627 (2019).
40. Fitzpatrick, A. W. P. et al. Cryo-EM structures of tau filaments from Alzheimer's disease. *Nature* **547**, 185–190 (2017).
41. Falcon, B. et al. Novel tau filament fold in chronic traumatic encephalopathy encloses hydrophobic molecules. *Nature* **568**, 420–423 (2019).
42. Wang, F. et al. Deterministic chaos in the self-assembly of β sheet nanotubes from an amphipathic oligopeptide. *Matter* **4**, 3217–3231 (2021).
43. To, W. S. & Midwood, K. S. Plasma and cellular fibronectin: distinct and independent functions during tissue repair. *Fibrogenesis Tissue Repair* **4**, 21 (2011).
44. Lu, Y. et al. Vacuolin-1 potently and reversibly inhibits autophagosome-lysosome fusion by activating RAB5A. *Autophagy* **10**, 1895–1905 (2014).
45. Du, X. et al. In situ generated D-peptidic nanofibrils as multifaceted apoptotic inducers to target cancer cells. *Cell Death Dis.* **8**, e2614–e2614 (2017).
46. Feng, Z., Wang, H., Chen, X. & Xu, B. Self-assembling ability determines the activity of enzyme-instructed self-assembly for inhibiting cancer cells. *J. Am. Chem. Soc.* **139**, 15377–15384 (2017).
47. Shigemitsu, H. et al. An adaptive supramolecular hydrogel comprising self-sorting double nanofibre networks. *Nat. Nanotechnol.* **13**, 165–172 (2018).
48. Epstein, I. R. & Xu, B. Reaction–diffusion processes at the nano- and microscales. *Nat. Nanotechnol.* **11**, 312–319 (2016).
49. Liang, G., Ren, H. & Rao, J. A biocompatible condensation reaction for controlled assembly of nanostructures in living cells. *Nat. Chem.* **2**, 54–60 (2010).
50. Engler, A. J., Sen, S., Sweeney, H. L. & Discher, D. E. Matrix elasticity directs stem cell lineage specification. *Cell* **126**, 677–689 (2006).

Methods

Materials and instruments

Details of this section are provided in the Supplementary Information.

Peptide synthesis (NBD–ffs$_p$y as an example)

All the peptides were synthesized according to standard solid-phase peptide synthesis procedures using 2-chlorotrityl resin. Fmoc-O-phospho-D-tyrosine and NBD–β-alanine were synthesized according to other works[51,52]. The peptides were cleaved using a cleavage cocktail (95.0% trifluoroacetic acid, 2.5% triisopropyl silane and 2.5% H_2O) for 1 h. After concentration, ice-cold ethyl ether was used for peptide precipitation. The crude peptides were purified by high-performance liquid chromatography.

Determination of critical micelle concentration

The critical micelle concentrations were determined using pyrene as an environment-sensitive probe[53]. Samples of a series of concentrations (3.1 μM to 2.0 mM) were prepared in pyrene-saturated PBS. The fluorescence emission spectrum of each concentration was collected. The peak intensities of 373 nm (I1) and 383 nm (I3) were obtained to calculate the I1/I3 value. The I1/I3 values were plotted against the concentrations of samples. The critical micelle concentration was determined as the intersection of two linear regression curves.

Rheology test

Time-dependent strain sweeps were conducted at room temperature on 400 μl NBD–ffs$_p$y (500 μM) with ALP (0.1 U ml^{-1}) in PBS at a frequency of 6.28 rad s^{-1} and strain of 0.1%, with a scanning frequency of 10 min per point. Frequency and strain sweeps were then conducted on the hydrogel formed. Frequency sweeps were conducted at a strain of 1%. Strain sweeps were conducted at a frequency of 6.28 rad s^{-1}.

TEM

Copper grids (400-mesh) coated with a carbon film were glow discharged at −20 mA for 30 s. Thereafter, 3 μl of the sample was loaded onto a grid and let to stand for 1 min. A filter paper was used to remove any excess of the sample. The sample was stained with 2% uranyl acetate for 20 s and then imaged on a Morgagni 268 TEM instrument at a high voltage of 80 kV.

Cryo-EM and image processing

The peptide nanofibre sample was applied to glow-discharged lacey carbon grids and vitrified using a plunge freezer (Leica) or a Vitrobot (Thermo Fisher). The grids were imaged on a Titan Krios (300 keV, Thermo Fisher) with a K3 camera (Gatan). Micrographs were collected under the electron-counting mode, using a defocus range of 1–2 μm with ~50 e^- Å^{-2} distributed into 40 fractions. Motion correction and contrast transfer function estimation were done in cryoSPARC[54–56]. The particles were auto-picked by 'filament tracer' with a shift of ~9 pixels. Non-peptide junk particles were removed by multiple rounds of reference-free two-dimensional classifications. Particles were kept if they had clear two-dimensional average patterns. On the basis of their shape and diameters, NBD–ffs$_p$y were then grouped into four different classes (class 1, class 2, class 3 and class 4). BP–ffsy, on the other hand, formed homogeneous nanofibres and only one type of fibre was observed. For each class of NBD–ffs$_p$y, the possible helical symmetries were calculated from an averaged power spectrum of the raw particles. All the possible symmetries were then tested by trial and error in cryoSPARC until the recognized peptide features, such as density of side chains, were observed. The resolution of each reconstruction was estimated by both map:map FSC and model:map FSC. The final volumes were then sharpened with a negative *B* factor automatically estimated in cryoSPARC, and the statistics are listed in Supplementary Tables 1 and 2.

Model building of NBD–ffsy filaments

The class 1 filament reached the highest resolution at ~3.1 Å among all the four different classes. The class 2 filament reached a resolution at ~3.2 Å based on map:map FSC. Since the NBD–ffsy filaments are made of only β sheets, the handedness of the helical map cannot be directly determined from the cryo-EM volume. This is unlike volumes that contain an α-helix in which the handedness is obvious when the resolution is 4.5 Å or better. In the published cross-β structures, the parallel β sheets typically have a left-handed twist. However, this observation may not be deducible to short peptides containing non-standard residues. Therefore, we performed the model building in both hands of the map of the class 1 filament. First, the model was manually adjusted in Coot[57] and then real-space refined in PHENIX[58]. It turned out that the model fits in a left-handed 10-start map slightly better than a right-handed 10-start map, with RSCC 0.89 versus 0.85 and Clashscore 22 versus 80. Therefore, we suggested that class 1 filament probably has a left-handed 10-start map. Similar procedures were performed for the class 2 filament. The class 3 and 4 filaments reach a moderate overall resolution of ~3.6 Å, but the resolution is not enough to determine the handedness of the map or build unambiguous atomic models. The resolutions for all the four classes and their refinement statistics are shown in Supplementary Table 1.

Model building of BP–ffsy filament

The handedness of the BP–ffsy filaments was determined in a similar approach as described above. According to map:map FSC, 3D reconstructions of BP–ffsy reach a 2.6 Å resolution. To refine the model into the cryo-EM map, we first made geometry restraints of the compound eLBOW. Then, the model was manually adjusted in Coot[57] and real-space refined in PHENIX[58]. The refinement statistics of both filaments are shown in Supplementary Table 2.

Cell culture

HS-5, HeLa, SJSA-1, SJSA-1–RFP, Saos-2, SKOV-3, PC-3, MCF-7, HepG2 and U-87 MG cells were purchased from ATCC, and OVSAHO cells were a gift from D. Dinulescu. TKO cells were a gift from P. D. Camilli's group. HeLa–GFP, Saos-2–GFP and PC-3–DsRed were a gift from J. T. Hsien. HS-5, HeLa, Saos-2 and HepG2 cell lines were authenticated by CellCheck 9—Human (9 marker STR profile and interspecies contamination test, IDEXX), confirming 100% match of the cell identity. HS-5 and TKO cells were cultured in DMEM supplemented with 10% fetal bovine serum (FBS). HeLa, HeLa–GFP and HepG2 cells were cultured in minimum essential medium supplemented with 10% FBS. SJSA-1, SJSA-1–RFP and OVSAHO cells were cultured in RPMI 1640 medium supplemented with 10% FBS. Saos-2 and Saos-2–GFP cells were cultured in McCoy's 5A medium supplemented with 15% FBS. SKOV-3 cells were cultured in McCoy's 5A medium supplemented with 10% FBS. U-87 MG cells were cultured in Eagle's minimum essential medium supplemented with 10% FBS. MCF-7 cells were cultured in Eagle's minimum essential medium supplemented with 10% FBS and 0.01 mg ml^{-1} human recombinant insulin. PC-3 and PC-3–DsRed cells were cultured in F-12K medium supplemented with 10% FBS. All the cell lines were supplemented with 100 U ml^{-1} penicillin and 100 μg ml^{-1} streptomycin and were cultured and humidified with 5% CO_2 at 37 °C.

Confocal microscopy of the spheroids

Adherent cells. Cells were seeded at 1.5×10^5 cells per dish on the inner 2.0 cm glass of a 3.5 cm confocal dish for 24 h to allow attachment. The peptide-containing fresh culture medium (500 μl) at a working concentration was directly prepared from the stock solution (10 mM) in PBS. After incubating the cells with the culture medium for a designated period of time, a live-cell imaging buffer was added to replace the culture medium. The cells were then used for live-cell imaging.

Suspended cells. Cells were treated with trypsin to obtain a cell suspension at a concentration of 1.5×10^5 cells per millilitre in the culture medium. A peptide stock solution was added into the culture medium to obtain a working solution with suspended cells. Cells were seeded at 7.5×10^4 cells per dish on the inner 2.0 cm glass of a 3.5 cm confocal dish for incubation. After incubating the cells for a designated period of time, a live-cell imaging buffer was added to replace the culture medium. The cells were then used for live-cell imaging.

Poly-D-lysine dish coating. In the biosafety cabinet, confocal dishes are coated with poly-D-lysine at the desired concentrations (0.050–50.0 μg ml^{-1}) by direct dilution from the stock solution (1 mg ml^{-1}) using sterile water. The confocal dishes are incubated at 37 °C for 1 h and the solution is aspirated. The dishes are then rinsed with sterile water and the surface is allowed to dry before cell seeding.

Hypoxia and live-/dead-cell staining of spheroids. HS-5 cells were seeded at a density of 7.5×10^4 cells per dish in the treatment of BP–ffs$_p$y (50 μM) and incubated for 72 h under normoxic conditions. The spheroids were then stained with a 5 μM hypoxia probe and 1 μg ml^{-1} Hoechst 33342 for 1 h for hypoxia staining or 2 μM calcein AM and 4 μM ethidium homodimer-1 for 1 h for live-/dead-cell imaging, respectively.

Immunofluorescence staining. The process is as follows: remove the culture media from the cells and wash twice with PBS. The cells were fixed with warm 4% paraformaldehyde for 15 min and permeabilized with 0.1% Triton X-100 in PBS for 10 min. Image-iT FX signal enhancer was added and incubated for 30 min to eliminate non-specific binding with the dye molecules. The cells were then blocked with 3% bovine serum albumin in PBS for 1 h at room temperature. Cells were stained with primary antibodies at distinct dilution in 1% bovine serum albumin in PBS overnight at 4 °C, and then incubated with Alexa Fluor-conjugated secondary antibody at a dilution of 1:1,000 for 1 h at room temperature. The nuclei were stained with 1 μg ml^{-1} of Hoechst 33342 in PBS for 15 min and washed with PBS three times after each step, except after blocking, where the primary antibodies were directly added.

Dilution for the primary antibodies: laminin, 1:100; fibronectin, 1:200; E-cadherin, 1:50; N-cadherin, 1:100; integrin alpha 5, 1:250; integrin beta 1, 1:200; integrin beta 3, 1:200; collagen I, 1:100; collagen III, 1:100; collagen IV, 1:100; EGFR, 1:200, TGFβ1, 1:200; Alexa Fluor 633 phalloidin, 5 U ml^{-1} (without the incubation of the secondary antibody).

Determination of dephosphorylation by ALP. NBD–ffs$_p$y (500 μM) was incubated with ALP (0.1 or 1 U ml^{-1}) in PBS for different periods of time and quenched with an equal volume of methanol. High-performance liquid chromatography was used to determine the dephosphorylation of NBD–ffs$_p$y.

Determination of dephosphorylation by cells

In conditioned media. Cells were seeded at 1.5×10^4 cells per well in a 96-well plate overnight to allow attachment. The cells were incubated with 100 μl NBD–ffs$_p$y (500 μM) for different periods of time, and their conditioned media were collected, lyophilized and then redissolved using methanol. High-performance liquid chromatography was used to determine the dephosphorylation of NBD–ffs$_p$y in the conditioned media.

In spheroids. Suspended HS-5 cells were seeded in NBD–ffs$_p$y (500 μM) containing culture media at 7.5×10^4 cells per dish in the inner 2.0 cm glass of a 3.5 cm confocal dish. The conditioned media and suspended cell spheroids were transferred and cell spheroids were collected by centrifugation. The supernatant was discarded and the cells were washed twice with PBS. The pellet was lyophilized and dissolved in methanol for liquid chromatography–mass spectrometry analysis.

Conditional dynamin I/II/III TKO of fibroblast. This protocol was developed by P. D. Camilli's group at Yale University School of Medicine (https://doi.org/10.17504/protocols.io.b2ddqa26). Here we show it in detail for clarity. When cells reach 80–90% confluency, we detach the cells using trypsin–EDTA and split the cells 1:4. We add 2 μM 4-hydroxytamoxifen in a fresh culture medium and incubate for 48 h. We then split the cells 1:4 once again after 48 h. Then, 300 nM 4-hydroxytamoxifen is added in fresh culture media and incubated for 72 h. Most of the dynamin disappears within the first 72–96 h, but the full phenotype appears 120–144 h after starting the 4-hydroxytamoxifen treatment. The knockout efficiency is around 90%. Here we seeded the cells for experiments 120 h after the tamoxifen treatment. A dish of cells without 4-hydroxytamoxifen treatment is used as a control.

LAMP1–RFP transduction. HS-5 cells were seeded in a confocal dish with the addition of lysosome–RFP at a concentration of 2 μl per 10,000 cells in DMEM and incubated for 24 h to allow attachment and transduction. It was replaced with fresh media containing NBD–ffs$_p$y (500 μM) and a different exocytosis inhibitor for live-cell imaging.

MTT assay. Cells were seeded at 10^4 cells per well in 96-well plates for 24 h to allow attachment. Culture media were replaced with fresh culture media supplemented with compounds at a series of concentrations. After 24/48/72 h, 10 μl of MTT solution (5 mg ml^{-1}) was added to each well and the plate was incubated in the dark for 4 h at 37 °C. Then, 100 μl of 10% sodium dodecyl sulfonate–HCl was added to each well to stop the reaction and dissolve the formazan. The absorbance of each well at 595 nm was determined by a microplate reader. The assay was performed three times to obtain the mean value of three measurements. For seven-day cytotoxicity, the cells were seeded at 5,000 cells per well and replaced with D-peptide-containing fresh medium every three days.

FRAP assay. FRAP was performed on a Zeiss LSM 880 confocal microscope using a 40×/1.4 oil objective. Five pre-bleach images were collected followed by photobleaching with a 488 nm laser at 100% intensity within a circular region (diameter, ~6 μm). Another region was imaged without photobleaching as an internal control. Here 512 × 512 pixel images were captured at 0.26 s intervals using the 488 nm laser at 1% intensity with the pinhole set at 390 μm. The images were collected until no further recovery was evident. The fluorescence recovery of the photobleached region was normalized and fitted into an exponential function.

Western blot. Cells were cultured to reach 80–90% confluency, lysed with 500 μl lysis buffer (protease inhibitor cocktail added) per 10 cm dish on ice, sonicated for 10 s and freeze–thawed for three cycles to collect cell lysates from various cell lines. The lysates were centrifuged at 15,294×*g* for 10 min at 4 °C, and the supernatant was collected. The proteins in the lysates were denatured by adding a sample loading buffer and incubated at 95 °C for 5 min. The lysate samples were loaded onto precast gels for electrophoresis under 120 V for 45 min, followed by blotting to a poly(vinylidene fluoride) membrane under 100 V for 90 min in an ice bath. The membranes were blocked with a blocking buffer for 1 h at room temperature and incubated with the primary antibody (1:1,000 dilution) at 4 °C overnight. After washing with TBS, supplemented with 0.1% Tween 20 (TBST) three times for 5 min per time, the secondary antibody was added at 1:5,000 dilution for 1 h at room temperature. After washing with TBST for six times, a chemiluminescent substrate was added and incubated for 1 min. The membranes were then scanned using a blot scanner. After scanning and washing the membranes with TBST, the antibodies on the membranes were stripped by incubation in a stripping buffer for 20 min. The membranes were then washed with TBST and blocked with a blocking buffer for 1 h at room temperature. The membranes were ready for the next round of primary antibody incubation.

Statistics and reproducibility

All the results are presented as mean ± standard deviation (s.d.). The sample sizes are indicated in the figure legends.

Experiments in Figs. 1c, 3a–c,l,m, 4e,f, 5d,g,h and 6n and Supplementary Figs. 19b,c, 20, 22d,e, 25a, 26a, 27b, 28e, 29b,e, 34c, 40c and 41b,d were repeated twice taken from distinct samples. Experiments in Figs. 1f, 3d,i,j,n, 5a,d and 6a,e,j,m,o,p and Supplementary Figs. 19a, 21a,b, 24a,b, 27a, 28b–d, 29a,c, 30a,b, 31a–f, 34a, 35, 36a,b, 37, 38a–c, 40a, 42a and 43 were repeated three times taken from distinct samples. The experiment in Fig. 2a,b was repeated to obtain 7,680 and 20,808 micrographs of the cryo-EM images, respectively.

Reporting summary

Further information on research design is available in the Nature Portfolio Reporting Summary linked to this article.

Data availability

The cryo-EM models of the structures reported in this study are deposited in the Protein Data Bank (PDB) under deposition ID 7L17 for class 1 NBD–ffsy filaments, 8DST for class 2 NBD–ffsy filaments and 8FOF for BP–ffsy filaments. The data generated in this study are available in the Article and its Supplementary Information. Source data are provided with this paper.

References

51. Ottinger, E. A., Shekels, L. L., Bernlohr, D. A. & Barany, G. Synthesis of phosphotyrosine-containing peptides and their use as substrates for protein tyrosine phosphatases. *Biochemistry* **32**, 4354–4361 (1993).
52. Liu, S. et al. Enzymatically forming intranuclear peptide assemblies for selectively killing human induced pluripotent stem cells. *J. Am. Chem. Soc.* **143**, 15852–15862 (2021).
53. Basu Ray, G., Chakraborty, I. & Moulik, S. P. Pyrene absorption can be a convenient method for probing critical micellar concentration (cmc) and indexing micellar polarity. *J. Colloid Interface Sci.* **294**, 248–254 (2006).
54. Rohou, A. & Grigorieff, N. CTFFIND4: fast and accurate defocus estimation from electron micrographs. *J. Struct. Biol.* **192**, 216–221 (2015).
55. Zheng, S. Q. et al. MotionCor2: anisotropic correction of beam-induced motion for improved cryo-electron microscopy. *Nat. Methods* **14**, 331–332 (2017).
56. Punjani, A., Zhang, H. & Fleet, D. J. Non-uniform refinement: adaptive regularization improves single-particle cryo-EM reconstruction. *Nat. Methods* **17**, 1214–1221 (2020).
57. Emsley, P. & Cowtan, K. Coot: model-building tools for molecular graphics. *Acta Crystallogr. D* **60**, 2126–2132 (2004).
58. Afonine, P. V. et al. Real-space refinement in PHENIX for cryo-EM and crystallography. *Acta Crystallogr. D* **74**, 531–544 (2018).

Acknowledgements

This work was partially supported by National Institutes of Health (NIH) grants CA142746 (B.X.), GM122510 (E.H.E.) and GM138756 (F.W.), as well as NSF grant DMR-2011846 (B.X.). This research was, in part, supported by the National Cancer Institute's National Cryo-EM Facility at the Frederick National Laboratory for Cancer Research under contract 75N91019D00024. The cryo-EM imaging was, in part, done at the Molecular Electron Microscopy Core Facility at the University of Virginia. The cryo-EM screening process was, in part, supported by the O'Neal Comprehensive Cancer Center at the University of Alabama at Birmingham. We thank P. D. Camilli for providing the TKO cell line. We thank J. T. Hsien for providing HeLa–GFP, PC-3–DsRed and Saos-2–GFP.

Author contributions

B.X. and J.G. conceived the study. J.G., under the supervision of B.X., designed and performed the chemical synthesis, generated the images in cell-free and cell-based assays and analysed the results. Y.H. and M.Y. assisted in the chemical synthesis. H.H. and W.T. performed the liquid chromatography–mass spectrometry analysis. F.W. and E.H.E. performed the cryo-EM reconstructions and model building. J.G., F.W., E.H.E. and B.X. wrote the manuscript with inputs from all authors.

Competing interests

The authors declare no competing interests.

Additional information

Supplementary information The online version contains supplementary material available at https://doi.org/10.1038/s41565-023-01401-7.

Correspondence and requests for materials should be addressed to Fengbin Wang, Edward H. Egelman or Bing Xu.

Peer review information *Nature Nanotechnology* thanks Deling Kong and the other, anonymous, reviewer(s) for their contribution to the peer review of this work.

nature portfolio

Corresponding author(s): Bing Xu
Edward H. Egelman
Fengbin Wang

Last updated by author(s): Mar 31, 2023

Reporting Summary

Nature Portfolio wishes to improve the reproducibility of the work that we publish. This form provides structure for consistency and transparency in reporting. For further information on Nature Portfolio policies, see our Editorial Policies and the Editorial Policy Checklist.

Statistics

For all statistical analyses, confirm that the following items are present in the figure legend, table legend, main text, or Methods section.

n/a	Confirmed	
☐	☒	The exact sample size (*n*) for each experimental group/condition, given as a discrete number and unit of measurement
☐	☒	A statement on whether measurements were taken from distinct samples or whether the same sample was measured repeatedly
☒	☐	The statistical test(s) used AND whether they are one- or two-sided *Only common tests should be described solely by name; describe more complex techniques in the Methods section.*
☒	☐	A description of all covariates tested
☒	☐	A description of any assumptions or corrections, such as tests of normality and adjustment for multiple comparisons
☐	☒	A full description of the statistical parameters including central tendency (e.g. means) or other basic estimates (e.g. regression coefficient) AND variation (e.g. standard deviation) or associated estimates of uncertainty (e.g. confidence intervals)
☒	☐	For null hypothesis testing, the test statistic (e.g. *F*, *t*, *r*) with confidence intervals, effect sizes, degrees of freedom and *P* value noted *Give P values as exact values whenever suitable.*
☒	☐	For Bayesian analysis, information on the choice of priors and Markov chain Monte Carlo settings
☒	☐	For hierarchical and complex designs, identification of the appropriate level for tests and full reporting of outcomes
☐	☒	Estimates of effect sizes (e.g. Cohen's *d*, Pearson's *r*), indicating how they were calculated

Our web collection on statistics for biologists contains articles on many of the points above.

Software and code

Policy information about availability of computer code

Data collection	HPLC was conducted on a reverse phase HPLC (Agilent 1100 Series) LC-MS spectra were obtained on a Waters Acquity Ultra Performance Liquid Chromatography with Waters Micromass Quattro Mass Spectrometer. TEM was conducted on Morgagni 268 transmission electron microscope. Cryo-EM was conducted on the state of art microscope Titan Krios (Thermo Fisher) equipped with a K3 direct electron camera (Gatan). CLSM was conducted on a Zeiss LSM 880 confocal microscopy. Fluorescence emission spectra were obtained on a Shimadzu RF-5301PC spectrometer. Rheology tests were conducted on a TA ARES-G2 rheometer at 25 degree Celsius. Western blot scanning was conducted on a LI-COR C-DiGit Blot Scanner.
Data analysis	Cryo-EM image processing was done in cryoSPARC. Cryo-EM model building was first manually adjusted in Coot and then real-space refined in PHENIX. 3D rendering, Z-projection, spatial fluorescence intensity profiles were generated using ZEN (black edition). Blot scans were analyzed using Imaging Studio 3.1. Colocalization scatter plots and coefficients were generated using ImageJ. Normalization, model/function fitting, and data plotting were conducted in Prism 7.

For manuscripts utilizing custom algorithms or software that are central to the research but not yet described in published literature, software must be made available to editors and reviewers. We strongly encourage code deposition in a community repository (e.g. GitHub). See the Nature Portfolio guidelines for submitting code & software for further information.

Data

Policy information about availability of data

All manuscripts must include a data availability statement. This statement should provide the following information, where applicable:

- Accession codes, unique identifiers, or web links for publicly available datasets
- A description of any restrictions on data availability
- For clinical datasets or third party data, please ensure that the statement adheres to our policy

The cryo-EM models of structures reported in this study are deposited to Protein Data Bank (PDB) under the deposition ID 7T6E for class 1 NBD-ffsy filaments, 8DST for class 2 NBD-ffsy filaments, and 8FOF for BP-ffsy filaments. The data generated in this study are available in the article and Supplementary Information. Source data are provided with this paper.

Field-specific reporting

Please select the one below that is the best fit for your research. If you are not sure, read the appropriate sections before making your selection.

☒ Life sciences ☐ Behavioural & social sciences ☐ Ecological, evolutionary & environmental sciences

For a reference copy of the document with all sections, see nature.com/documents/nr-reporting-summary-flat.pdf

Life sciences study design

All studies must disclose on these points even when the disclosure is negative.

Sample size	No sample size calculation during experiment design. For colocalization analysis, refer to Cell Death Dis 12, 657 (2021). For MTT assay, refer to J. Am. Chem. Soc. 2016, 138, 49, 16046–16055. For individual cells, spheroids and nanofibers, at least 10 independent samples were analyzed to generate mean value and standard deviation. For cryo-EM structural determination, more than half million particle images were collected for model building. The sample sizes in this study are indicated in the figure legends.
Data exclusions	The nonspecific binding bands in Western Blot were excluded from quantification.
Replication	All the cell-based and cell-free experiments were repeated two to three times. Details of reproducibility can be found in the “Statistics and Reproducibility" in Methods section.
Randomization	All cells were randomly allocated to each group before treatment.
Blinding	Investigators were not blinded for the experiments because the they need to keep track on multiple steps (peptide synthesis, cell culture, data collection and data analysis).

Reporting for specific materials, systems and methods

We require information from authors about some types of materials, experimental systems and methods used in many studies. Here, indicate whether each material, system or method listed is relevant to your study. If you are not sure if a list item applies to your research, read the appropriate section before selecting a response.

Materials & experimental systems

n/a	Involved in the study
☐	☒ Antibodies
☐	☒ Eukaryotic cell lines
☒	☐ Palaeontology and archaeology
☒	☐ Animals and other organisms
☒	☐ Human research participants
☒	☐ Clinical data
☒	☐ Dual use research of concern

Methods

n/a	Involved in the study
☒	☐ ChIP-seq
☒	☐ Flow cytometry
☒	☐ MRI-based neuroimaging

Antibodies

Antibodies used	Laminin polyclonal antibody (catalog # PA1-16730), fibronectin polyclonal antibody (catalog # PA5-29578), collagen III polyclonal antibody (catalog # PA5-34787), collagen I polyclonal antibody (catalog # PA1-26204), collagen IV polyclonal antibody (catalog # PA5-104508), EGFR polyclonal antibody (catalog # PA1-1110), TGF beta-1 polyclonal antibody (catalog # PA1-29032), integrin alpha 5 polyclonal antibody (catalog # PA5-79529), placental alkaline phosphatase recombinant rabbit monoclonal antibody (catalog #

MA5-41235), E-cadherin polyclonal antibody (catalog # 20874-1-AP), N-cadherin polyclonal antibody (catalog # PA5-19486), goat anti-rabbit IgG (H+L) secondary antibody, HRP (catalog # 31460), goat anti-rabbit IgG (Heavy chain), superclonal™ recombinant secondary antibody, Alexa Fluor™ 647 (catalog # A27040) were purchased from Thermo Fisher.
Anti-beta actin antibody (catalog # ab8227), recombinant anti-integrin beta 1 antibody (catalog # ab52971), anti-integrin beta 3 antibody (catalog # ab197662), anti-intestinal alkaline phosphatase antibody (catalog # ab70975), anti-alkaline phosphatase, tissue non-specific antibody (catalog # ab108337), and goat anti-rabbit IgG H&L (Alexa Fluor® 488) (catalog # ab150077) were purchased from Abcam.
Dynamin I/II polyclonal antibody (catalog # 2342S) was purchased from cell signaling technology.

Validation

The validation of antibodies were verified by the suppliers (Thermo Fisher, Abcam, cell signaling technology), with the results available on the manufacturer's website. No further verification was performed.

Eukaryotic cell lines

Policy information about cell lines

Cell line source(s)

HS-5, HeLa, SJSA-1, SJSA-1-RFP, Saos-2, SKOV-3, PC-3, MCF-7, HepG-2, and U-87 MG cells were purchased from ATCC, OVSAHO cells were given by Dr. Daniela Dinulescu.
TKO cells were given by Prof. Pietro De Camilli group. HeLa-GFP, Saos-2-GFP, and PC-3-DsRed were given by Dr. J. T. Hsien.

Authentication

HS-5, HeLa, Saos-2, and HepG-2 cell lines were authenticated by CellCheck 9 - human (9 Marker STR Profile and Inter-species Contamination Test, IDEXX), confirming 100% match of the cell identity.

Mycoplasma contamination

All cell lines were tested negative for Mycoplasma contamination.

Commonly misidentified lines
(See ICLAC register)

No misidentified cell lines were used.